Slat Noise Source Identification for a High-Lift Configuration

D. König[1], S. R. Koh, W. Schröder, M. Meinke
Institute of Aerodynamics, RWTH Aachen University, Wüllnerstraße 5a, D-52062 Aachen, Germany
[1] *Email: d.koenig@aia.rwth-aachen.de*

Introduction

Since quite some progress has been made in the reduction of jet noise airframe noise has become more or more important over the last couple of years. Especially during landing, when engines run almost in idle condition, airframe noise is an essential part of the emitted sound. The major contributors of airframe noise are high-lift devices, like slats and flaps, and landing gears. Increasing air traffic and stricter regulations require a low noise design of these airplane parts. To achieve this objective the detailed understanding of the underlying sound generating turbulent flow field is necessary.

First measurements concerning slat noise have been performed by Pott-Pollenske et al. [18]. Their investigations show that the emitted sound spectra consists of broadband and tonal noise components. Kolb et al. [14] discuss the tonal components occurring in the low frequency range between 1kHz and 3kHz to be similar to the Rossiter modes known from cavity flow. That is, the slat cove is interpreted to have a cavity-like geometry. In recent years various numerical investigations of slat flow have been performed, e.g., based on unsteady Reynolds-averaged Navier-Stokes (RANS) simulations [11, 12, 4, 13] or using hybrid methods based on a combined Reynolds-averaged Navier-Stokes and large-eddy simulation (LES) [9, 17]. However, no thorough analysis of a noise-flow relationship has been given. Therefore, in the present study the turbulent flow field over a slat-main-wing configuration and the associated acoustic field examined to identify the noise generating processes. The angle-of-attack is $\alpha = 13$ deg, the freestream Mach number is Ma=0.16 and the Reynolds number based on the freestream velocity and the clean chord length is Re=$1.4{\cdot}10^6$. Since a low Mach number flow is investigated the acoustic field is computed via efficient hybrid approach. That is, a two-step method using a large-eddy simulation for the flow field and acoustic perturbation equations (APE) for the acoustic field [5, 6] is used.

The paper is organized as follows. First, the numerical methods and the computational setups of the large-eddy simulation and the aeroacoustic simulation are briefly described. Subsequently, the mean and the unsteady flow field are presented. Finally, the acoustic field is analyzed including the use of cross-correlation functions of the acoustic pressure and the Lamb vector to identify and locate the dominant noise sources.

Numerical methods and computational setup

Large-eddy simulation

The three-dimensional unsteady compressible Navier-Stokes equations are solved based on a large-eddy simulation (LES) using a MILES (monotone integrated LES) approach [1]. The vertex-centered finite-volume flow solver is block-structured. A modified AUSM method is used for the formulation of the inviscid terms [15] which are discretized to second-order accuracy by an upwind-biased approximation. For the viscous terms a centered approximation of second-order is used. The temporal integration from time level n to $n+1$ is done by a second-order accurate explicit 5-stage Runge-Kutta method, the coefficients of which are optimized for maximum stability. For a detailed description of the flow solver the reader is referred to Meinke et al. [16].

The computational mesh used for the LES consists of 32 blocks with approximately 55 million grid points. The extent in the spanwise direction amounts to 2.1% of the clean chord length and is resolved by 65 points. Roughly 3000 and 280 cells are distributed in the streamwise and normal extension of the computational domain. Using the friction velocity $u_* = \sqrt{\tau_w/\rho}$ to define the non-dimensional inner coordinates $\Delta h_i^+ = \Delta h u_*/\nu$ the mesh resolution near the surface is $\Delta x^+ \approx 100$, $\Delta y^+ \approx 1$, and $\Delta z^+ \approx 22$. These values are approximated by the analytical solution of a flat plate during the grid generation process.

On the far-field boundaries of the computational domain boundary conditions based on the theory of characteristics are applied. A sponge layer [10] is imposed on these boundaries to avoid spurious reflections, which would affect the acoustic analyses. On the walls, an adiabatic no-slip boundary condition is applied with a zero pressure gradient normal to the wall. In the spanwise direction periodic boundary conditions are used.

Acoustic simulation

The acoustic analyses are done by solving the acoustic perturbation equations (APE) in the APE-4 formulation [5]. This system of equations possesses the same wave operator as the basic acoustic perturbation equations which have been derived by filtering the linearized conservation equations in the Fourier/Laplace space [5]. The left-hand side of the APE-4 formulation constitutes a linear system describing linear wave propagation in mean flows with convection and

refraction effects. The right-hand side represents the acoustic source terms. In this work only the perturbed Lamb vector $\vec{L}' = (\omega \times u)'$ is considered. That is, it is conjectured that vortex sound is the major contribution. The numerical algorithm to solve the APE-4 system is based on a 7-point finite-difference scheme using the dispersion-relation preserving scheme (DRP) [23] for the spatial discretization including the metric terms on curvilinear grids. This scheme accurately resolves waves longer than 5.4 points per wave length (PPW). For the time integration an alternating 5-6 stage low-dispersion low-dissipation Runge-Kutta scheme [8] is implemented. To eliminate spurious oscillations the solution is filtered using a 6th-order explicit commutative filter [22, 24] at every tenth iteration step. Since the APE system does not contain convection of entropy and vorticity perturbations [5] the asymptotic radiation boundary condition by Tam and Webb [23] is sufficient to minimize reflections on the outer boundaries. On the inner boundaries between the differently resolved LES and acoustic domains, where the transition of the inhomogeneous to the homogeneous acoustic equations takes place, a damping zone is formulated to suppress artificial noise generated by a possible discontinuity in the vorticity distribution [21].
The two-dimensional acoustic mesh for the APE solution has a total number of 1.8 million grid points. This 2D-formulation is due to the fact that especially at low Mach number flows the turbulent length scales are significantly smaller than the acoustic length scales and as such the noise sources can be considered compact. This treatment tends to result in somewhat overpredicted sound pressure levels which can be corrected following the method described by Ewert et al. [7].

Results

The discussion of the results starts with the time and spanwise averaged flow field. Figure 1 shows the Mach number distribution and some selected streamlines which clearly identify the existence of a recirculation area in the slat cove region. This recirculation region is separated from the flow passing the slat gap by a shear layer emanating from the slat cusp and reattaching short upstream of the upper slat trailing edge. The LES pressure distribution compared to a two-dimensional RANS simulation and experimental findings is depicted in Fig. 2. The RANS results match the measurements somewhat better. This is due to the limited spanwise extent of the LES domain and is a direct result of the angle-of-attack correction, which was determined based on RANS computations. In other words, the RANS computation has been adjusted to the experimental distribution via modifying the angle-of-attack. In Fig. 3 the turbulent kinetic energy k=$\frac{1}{2}{u'_{ii}}^2$ is shown. In agreement with the findings of Choudhari and Khorrami [4] the maximum peaks occur in the reattachment area of the slat cove shear layer and at the upper slat trailing edge. Figures 4 and 5 show snapshots of the turbulent flow structures visualized by λ_2 contours. Figure 4 reveals that turbulent structures occur mainly in the slat cove region and on the upper side of the slat and main wing. A closer look of the slat cove area in Fig. 5 identifies the existence of periodically appearing spanwise orientated rollers and streamwise aligned rib vortices in the slat cove shear layer. Similar structures have been observed in plane shear layers [19] and impinging jets [20]. When these structures approach the shear layer reattachment region they become highly deformed and stretched due to the accelerated slat gap flow and finally they are destroyed when impinging on the slat.
The acoustic field is shown in Fig. 6. It is obvious that the pressure fluctuations are mainly generated in the slat region and at the trailing edge of the main wing.
Figure 7 juxtapose the frequency spectra obtained via experimental measurements and numerical simulation for a microphone located at a distance $r = 3.53c$ from the upper slat trailing edge and an angle $\theta = 305$ deg. where c is the is chord length of the main wing and θ is defined counter-clockwise relative to the streamwise direction. Both results are in good agreement and show a mix of broadband and tonal noise. Also noticeable is the f^{-2} dependence of the power spectral density.
The dominant noise structures can be analyzed by a cross-correlation function R_{AB} between far-field acoustics and turbulent flow motion. Based on an evanescent-wave formulation Chase [3] has obtained the spectra of near-field surface pressure and of far-field acoustic pressure and the cross spectra between them. By measuring convecting surface pressure Brooks and Hodgson [2] have considered the turbulent coherence to refine the existing theory. Yu and Tam [25] have used a cross-correlation function to identify the noise sources and to understand the physical mechanism of sound generation from a turbulent wall jet interacting with a sharp trailing edge. In the present study the cross-correlation function is defined as

$$R_{AB}(\vec{\xi},\tau) = \frac{\overline{A(\vec{x},t)\,B(\vec{x}+\vec{\xi},t+\tau)}}{\sqrt{\overline{A(\vec{x},t)^2}}\sqrt{\overline{B(\vec{x},t)^2}}} \quad , \qquad (1)$$

where $\vec{x}$ and t define the origin of the correlation, $\vec{\xi}$ is the spatial distance, and τ is the time delay. Concerning the acoustic pressure signal determined at a microphone in the near far-field, the vortex sound source $\vec{L}' = (\vec{\omega} \times \vec{u})'$ is chosen for the cross-correlation function R_{AB} where the subscript A represents the acoustic pressure and the subscript B the noise source term, i.e., in the current analysis A is p' and B is $|\vec{L}'|$. In the present analysis the cross-correlation function is computed using a filtered version of the acoustic pressure signal. That is, a band-pass filter of shape factor 1.2:1 at 30/3dB is applied to the frequency domain and subsequently, the filtered signal is transformed back into the time domain. In the presented study a 2kHz band-pass filter at the center frequency of 2kHz is used which leads to an acoustic pressure signal containing only the noticeable tonal and broadband components between 1kHz and 3kHz. Figures 8 to 10 show that high values of the correlation function only occurs in the slat gap vicinity and at a time delay of $\tau \approx$

3.5. For a more thorough investigation the correlation functions for all time shifts τ are plotted in Fig. 11 for four points located at a distance of $1.6h$, $4.2h$, $10.5h$, and $14.6h$, respectively, from the slat trailing edge where h is the thickness of the trailing edge of the slat. It is obvious that the peak value, especially for point c, occur at a phase shift of $\tau \approx 3.5$. This is nearly exactly the time a signal traveling at the speed of sound a_∞ needs to cover the distance $|\vec{\xi}|$ between points A and B. Hence, the cross-correlation reveals the slat gap as a major contributor to the mixed tonal and broadband noise in the frequency range of 1 kHz to 3 kHz.

References

[1] Boris, J.P., Grinstein, F.F., Oran, E.S., Kolbe, R.L.: New insights into large eddy simulation. Fluid Dynamics Research **10**, 199–228 (1992)

[2] Brooks, T., Hodgson, T.: Trailing edge noise prediction from measured surface pressures. Journal of Sound and Vibration **78**, 69–117 (1981)

[3] Chase, D.: Noise radiated from an edge in turbulent flow. AIAA J. **13**, 1041–1047 (1975)

[4] Choudhari, M.M., Khorrami, M.R.: Slat cove unsteadiness: Effect of 3d flow structures. In: 44st AIAA Aerospace Sciences Meeting and Exhibit. AIAA Paper 2006-0211 (2006)

[5] Ewert, R., Schröder, W.: Acoustic perturbation equations based on flow decomposition via source filtering. J. Comput. Phys. **188**, 365–398 (2003)

[6] Ewert, R., Schröder, W.: On the simulation of trailing edge noise with a hybrid LES/RANS method. Journal of Sound and Vibration **270**, 509–524 (2004)

[7] Ewert, R., Zhang, Q., Schröder, W., Delfs, J.: Computation of trailing edge noise of a 3d lifting airfoil in turbulent subsonic flow. AIAA Paper 2003-3114 (2003)

[8] Hu, F.Q., Hussaini, M.Y., Manthey, J.L.: Low-dissipation and low-dispersion Runge-Kutta schemes for computational acoustics. J. Comput. Phys. **124**(1), 177–191 (1996)

[9] Imamura, T., Enomoto, S., Yokokawa, Y., Yamamoto, K.: Three-Dimensional Unsteady Flow Computations Around a Conventional Slat of High-Lift Devices. AIAA J. **46**(5), 1045–1053 (2008)

[10] Israeli, M., Orszag, S.A.: Approximation of radiation boundary conditions. J. Comput. Phys. **41**, 115–135 (1981)

[11] Khorrami, M.R., Berkman, M.E., Choudhari, M.: Unsteady flow computations of a slat with a blunt trailing edge. AIAA J. **38**(11), 2050–2058 (2000)

[12] Khorrami, M.R., Berkman, M.E., Li, F., Singer, B.A.: Computational simulations of a three-dimensional high-lift wing. In: 20th AIAA Applied Aerodynamics Conference. AIAA Paper 2002-2804 (2002)

[13] Knacke, T., Thiele, F.: Slat noise reduction using steady suction. In: 46th AIAA Aerospace Sciences Meeting and Exhibit. AIAA Paper 2008-17 (2008)

[14] Kolb, A., Faulhaber, P., Drobietz, R., Grünewald, M.: Aeroacoustic wind tunnel measurements on a 2d high-lift configuration. In: 13th AIAA/CEAS Aeroacoustics Conference AIAA. AIAA Paper 2007-3447 (2007)

[15] Liou, M.S., Steffen, C.J.: A new flux splitting scheme. J. Comput. Phys. **107**, 23–39 (1993)

[16] Meinke, M., Schröder, W., Krause, E., Rister, T.: A comparison of second- and sixth-order methods for large-eddy simulations. Computers and Fluids **31**, 695–718 (2002)

[17] Mockett, C., Greschner, B., Knacke, T., Perrin, R., Yan, J., Thiele, F.: Demonstration of improved DES methods for generic and industrial applications. In: Advances in Hybrid RANS-LES Modelling, *Notes on Numerical Fluid Mechanics and Multidisciplinary Design*, vol. 97, pp. 222–231. Springer Berlin, Heidelberg (2008)

[18] Pott-Pollenske, M., Alvarez-Gonzalez, J., Dobrzynski, W.: Effect of slat gap on farfield radiated noise and correlation with local flow characteristics. In: 9th AIAA/CEAS Aeroacoustics Conference. AIAA Paper 2003-3228 (2003)

[19] Rogers, M.M., Moser, R.D.: The three-dimensional evolution of a plane mixing layer: the Kelvin-Helmholtz rollup. J. Fluid Mech. **243**, 183–226 (1992)

[20] Sakakibara, J., Hishida, K., Phillips, W.R.C.: On the vortical structure in an plane impinging jet. J. Fluid Mech. **434**, 273–300 (2001)

[21] Schröder, W., Ewert, R.: LES for Acoustics, LES-CAA Coupling. Cambridge University Press (2005)

[22] Shang, J.S.: High-order compact-difference schemes for time dependent maxwell equations. J. Comput. Phys. **153**, 312–333 (1999)

[23] Tam, C.K.W., Webb, J.C.: Dispersion-relation-preserving finite difference schemes for computational acoustics. J. Comput. Phys. **107**(2), 262–281 (1993)

[24] Vasilyev, O.V., Lund, T.S., Moin, P.: A general class of commutative filters for LES in complex geometries. J. Comput. Phys. **146**, 82–104 (1998)

[25] Yu, J.C., Tam, C.K.W.: An experimental investigation of the trailing edge noise mechanism. AIAA J. **16**, 1046–1052 (1978)

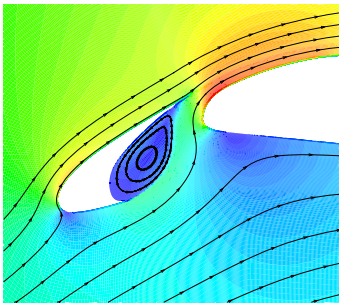

Figure 1: Streamlines and Mach number contours of the time and spanwise averaged LES flow field data in the slat area.

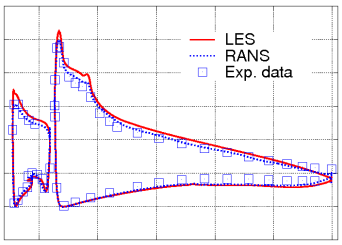

Figure 2: Pressure distribution c_p: LES, RANS, and measurement.

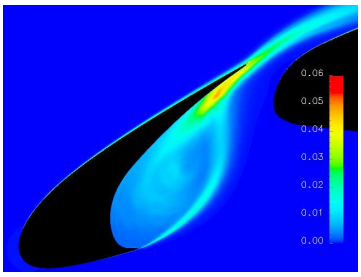

Figure 3: Turbulent kinetic energy k non-dimensionalized by u_∞^2 in the slat cove region.

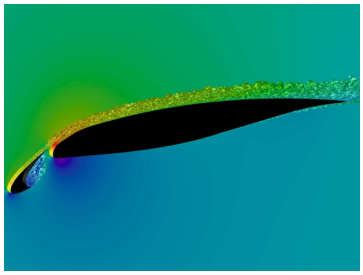

Figure 4: Turbulent structures visualized by λ_2 contours with mapped on Mach number distribution.

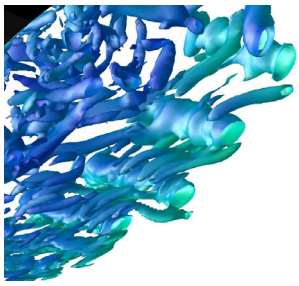

Figure 5: λ_2 contours show rollers and streamwise rib vortices in the shear layer.

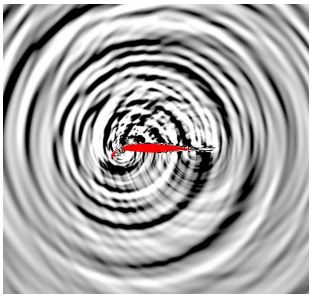

Figure 6: Pressure contours based on the LES/APE solution.

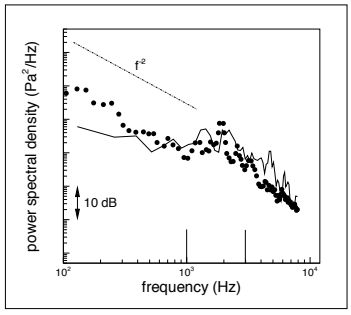

Figure 7: Sound spectrum at a microphone postion in the near far-field. Solid line: computation, symbol: experiment. Vertical lines mark the 1 to 3kHz range in which tonal and broadband noise is noticeable.

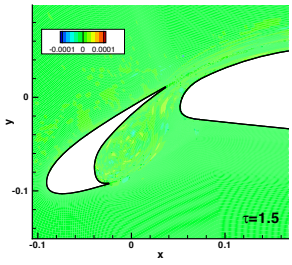

Figure 8: Cross-correlation contours of $R_{AB}(\vec{\xi}, \tau = 1.5)$ determined by the acoustic source $|L'|$ and the filtered acoustic pressure p'.

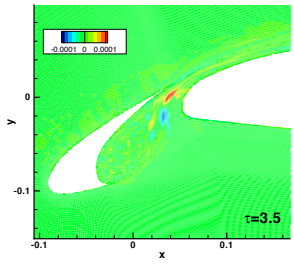

Figure 9: Cross-correlation contours of $R_{AB}(\vec{\xi}, \tau = 3.5)$ determined by the acoustic source $|L'|$ and the filtered acoustic pressure p'.

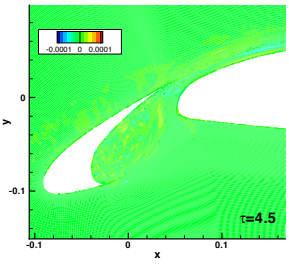

Figure 10: Cross-correlation contours of $R_{AB}(\vec{\xi}, \tau = 4.5)$ determined by the acoustic source $|L'|$ and the filtered acoustic pressure p'.

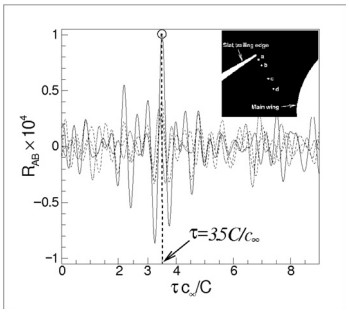

Figure 11: Temporal distribution of R_{AB} at four locations 'a' $\cdots$, 'b' $-\cdot-$, 'c' ——, 'd' $- - -$, which are defined in the upper subfigure.